

This is the accepted manuscript made available via CHORUS. The article has been published as:

Valley plasmonics in transition metal dichalcogenides

R. E. Groenewald, M. Rösner, G. Schönhoff, S. Haas, and T. O. Wehling

Phys. Rev. B **93**, 205145 — Published 25 May 2016

DOI: [10.1103/PhysRevB.93.205145](https://doi.org/10.1103/PhysRevB.93.205145)

Valley Plasmonics in Transition Metal Dichalcogenides

R. E. Groenewald,^{1,*} M. Rösner,^{2,3,*} G. Schönhoff,^{2,3} S. Haas,¹ and T. O. Wehling^{2,3}

¹*Department of Physics and Astronomy, University of Southern California, Los Angeles, CA 90089-0484, USA*

²*Institut für Theoretische Physik, Universität Bremen, Otto-Hahn-Allee 1, 28359 Bremen, Germany*

³*Bremen Center for Computational Materials Science,
Universität Bremen, Am Fallturm 1a, 28359 Bremen, Germany*

The rich phenomenology of plasmonic excitations in the dichalcogenides is analyzed as a function of doping. The many-body polarization, the dielectric response function and electron energy loss spectra are calculated using an ab initio based model involving material-realistic Coulomb interactions, band structure and spin-orbit coupling. Focusing on the representative case of MoS₂, a plethora of plasmon bands are observed, originating from scattering processes within and between the conduction or valence band valleys. We discuss the resulting square-root and linear collective modes, arising from long-range versus short-range screening of the Coulomb potential. We show that the multi-orbital nature of the bands and spin-orbit coupling strongly affects *inter-valley* scattering processes by gapping certain two-particle modes at large momentum transfer.

I. INTRODUCTION

Collective excitations are of great interest in low-dimensional materials which are characterized by reduced dielectric screening of Coulomb interactions. As a prominent example, plasmon modes in layered systems might form the basis to build optical devices, wave guides or so called plasmonic circuits¹⁻⁴. In two dimensions (2d) the plasmonic dispersion exhibits a characteristic low-energy acoustic mode $\omega(q) \propto \sqrt{q}$ originating from low-momentum electron scattering^{5,6}, which has been observed experimentally^{7,8} and studied extensively from a theoretical point of view^{3,9-12} in graphene. Furthermore, it has been predicted that additional linear plasmons with $\omega(q) \propto q$ arise due to high-momentum scattering processes between degenerated valleys such as K and K' in graphene¹³. Coupling of the electrons with such intrinsic gapless bosonic modes may lead to instabilities, such as charge density wave and superconducting phases¹⁴⁻¹⁷, similar to the effect of phonons.

An analogous but even richer phenomenology can be expected in the structurally related monolayer transition metal dichalcogenides (TMDCs) MX₂, where M stands for a transition metal and X for a chalcogen atom. These materials host rich plasmonic physics including an interplay of plasmons with charge density waves¹⁸⁻²⁰ and first plasmon based applications have already been proposed²¹⁻²³.

Here we focus on the representative example of doped MoS₂ whose low-energy band structure can be described by three effective tight-binding bands. These originate mostly from the Mo d orbitals, giving rise to prominent valleys at wave vectors K and Σ in the lowest conduction band as well as at K in the highest valence band²⁴⁻²⁶, leading to Fermi surfaces as sketched out in Fig. 1. Furthermore, there is substantial spin-orbit coupling (SOC) in these materials²⁷, with a primary effect on the low-energy physics by introducing a splitting of the Σ valleys in the lowest conduction band and of the K valleys in the highest valence band. Although all of these Fermi

surface characteristics can be experimentally sampled by means of field effect electron or hole doping²⁸, the resulting impact to the plasmonic dispersions is not known.

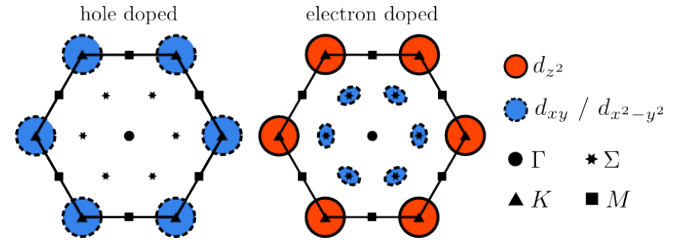


Figure 1: (Color online) Sketch of the Fermi surfaces in hole doped (left) and electron doped (right) monolayer MoS₂. The predominant orbital-character weights of each surface is indicated by red (d_{z^2}) and blue (d_{xy} and $d_{x^2-y^2}$) fillings. Points of high symmetry are indicated by different markers.

To close this gap, we present an extensive study of the plasmon dispersion at arbitrary momenta along paths throughout the whole Brillouin zone for different doping levels. Specifically we are interested in *inter-valley* plasmons which have not been studied in TMDCs so far. In order to highlight the multi-orbital character of the Fermi surface (see Fig. 1) and the presence of spin-orbit coupling we consider hole and electron doped cases. In the hole doped example we show how spin-orbit coupling affects the *inter-valley* plasmons while the electron doped case is used to study the influence of the multi pocket structure of the Fermi surface. Thereby we gain a comprehensive and realistic picture of the most important contributions to the *low energy* plasmon modes in monolayer TMDCs.

II. METHODS

The collective plasmon modes are described by the polarization and dielectric functions, which we evaluate in several steps, starting with a G_0W_0 calculation to deter-

mine the electronic band structure for the *undoped* system. We then obtain an effective 3-band model by projecting to a Wannier basis spanned by the Mo $d_{x^2-y^2}$, d_{xy} and d_{z^2} orbitals, which has been found to accurately describe the highest valence band and the two lowest conduction bands with tight-binding hopping matrix elements $t_{\alpha\beta}$, where α and β are the orbital indices (see Appendix A). The same projection is used to obtain the static part of the Coulomb interaction in the Wannier basis, which is screened by *all* bands including those, which are not included in the minimal 3-band-model⁴⁷.

This procedure leads to an effective material-specific model with screened Coulomb $U_{\alpha\beta\gamma\delta}$ and hopping $t_{\alpha\beta}$ matrix elements in the orbital basis, describing the undoped system in its ground state. We find that this treatment is essential to derive material realistic plasmonic dispersions upon doping. In contrast to simplified $k \cdot p$ models^{29,30}, which utilize *bare* Coulomb matrix elements at this stage, our interaction matrix elements are strongly reduced due to screening effects from the electronic bands which are neglected in the $k \cdot p$ models (see Appendix B for comparisons). As a result of the 2d layer geometry, these dielectric properties cannot be modeled by a simple dielectric *constant* but have to be described as a \mathbf{q} -dependent dielectric *function*^{31,32}.

In order to obtain the dynamic response in the *doped* system, we determine the dynamic susceptibility within the 3-orbital basis by evaluating the polarization in the random phase approximation (RPA), which is given for a single spin channel σ by

$$\Pi_{\alpha\beta}^{\sigma}(\mathbf{q}, \omega) = \sum_{\lambda_1 \lambda_2 \mathbf{k}} \frac{M_{\alpha\beta}^{\lambda_1 \lambda_2} [f_{\lambda_2}^{\sigma}(\mathbf{k} + \mathbf{q}) - f_{\lambda_1}^{\sigma}(\mathbf{k})]}{\omega + i\delta + E_{\lambda_2}^{\sigma}(\mathbf{k} + \mathbf{q}) - E_{\lambda_1}^{\sigma}(\mathbf{k})}, \quad (1)$$

where \mathbf{q} and \mathbf{k} are wave vectors from the first Brillouin zone, λ_i band indices, $f_{\lambda_i}^{\sigma}(\mathbf{k})$ Fermi functions for the energies $E_{\lambda_i}^{\sigma}(\mathbf{k})$ and $i\delta$ a small broadening parameter. The overlap matrix elements are given by $M_{\alpha\beta}^{\lambda_1 \lambda_2} = \bar{c}_{\alpha}^{\lambda_1}(\mathbf{k}) c_{\beta}^{\lambda_2}(\mathbf{k}) \bar{c}_{\beta}^{\lambda_2}(\mathbf{k} + \mathbf{q}) c_{\alpha}^{\lambda_1}(\mathbf{k} + \mathbf{q})$, where $c_{\alpha}^{\lambda_i}(\mathbf{k})$ is the expansion coefficient of the eigenfunction corresponding to $E_{\lambda_i}^{\sigma}(\mathbf{k})$ in the orbital basis. Here, we already reduced the polarization tensor of 4th order to a matrix to describe density-density correlations only. Hence, we neglect orbital exchange (Fock-like) matrix elements as well as elements with three or even four different orbital contributions. A detailed analysis of the full background screened Coulomb tensor $U_{\alpha\beta\gamma\delta}$ shows that these elements are in general one order of magnitude smaller or even vanish due to symmetries, which convinces us to stay with density-density like elements.

Using the full density-density polarization $\Pi(\mathbf{q}, \omega) = \Pi^{\uparrow}(\mathbf{q}, \omega) + \Pi^{\downarrow}(\mathbf{q}, \omega)$ the dielectric function is obtained via the following matrix equation

$$\varepsilon(\mathbf{q}, \omega) = \mathbb{1} - U(\mathbf{q})\Pi(\mathbf{q}, \omega), \quad (2)$$

where the background screened Coulomb interaction enters via $U(\mathbf{q})$. By including an effective spin-orbit

coupling (SOC) as described in Ref.²⁶ the spin degeneracy is removed but time reversal symmetry is preserved. Then, the spin resolved band structure still obeys $E_{\lambda}^{\uparrow}(\mathbf{k}) = E_{\lambda}^{\downarrow}(-\mathbf{k})$ and the total polarization including the spin summation can be written as $\Pi(\mathbf{q}, \omega) = \Pi^{\uparrow}(\mathbf{q}, \omega) + \Pi^{\downarrow}(-\mathbf{q}, \omega)$.

The dielectric function describes the *screened* Coulomb matrix $V(\mathbf{q}, \omega) = \varepsilon^{-1}(\mathbf{q}, \omega)U(\mathbf{q})$ and implicitly defines the plasmonic dispersions by (\mathbf{q}, ω) pairs such that $\varepsilon_m(\mathbf{q}, \omega) = 0$. Here ε_m is the *macroscopic* part of the dielectric function defined in the orbital basis as the projection

$$\varepsilon_m(\mathbf{q}, \omega) = \langle v_1(\mathbf{q}) | \varepsilon(\mathbf{q}, \omega) | v_1(\mathbf{q}) \rangle, \quad (3)$$

where $|v_1(\mathbf{q})\rangle$ is the eigenfunction corresponding to the largest eigenvalue of the bare Coulomb interaction matrix $U(\mathbf{q})$ ³³. The most promising experimental method to measure these plasmon modes is electron energy loss spectroscopy (EELS), measuring the imaginary part of the inverse dielectric function

$$\text{EELS}(\mathbf{q}, \omega) = -\text{Im} \left(\frac{1}{\varepsilon_m(\mathbf{q}, \omega)} \right), \quad (4)$$

which is sensitive to both collective and single-particle excitations (visible as maxima in the EELS spectra)³⁴.

It is important to note that the RPA description of plasmonic properties involves solely Landau-damping processes due to excitations of single particle-hole pairs. In reality electron-impurity, electron-phonon³⁵ or electron-electron scattering³⁶ would yield additional damping effects which are phenomenologically included here due to the small but finite broadening parameter $\delta = 0.0005$ eV in Eq. (1). This broadening corresponds to plasmon lifetimes of about 1 ps which is on the same order as electron-electron scattering induced plasmonic lifetimes of a 2d electron gas and one to two orders of magnitude smaller than in freestanding doped graphene³⁶.

In comparison to other RPA based approaches (neglecting broadening effects) we find, that a material-realistic description of the Coulomb interaction of the undoped system [rendered in $U(\mathbf{q})$] in combination with highly accurate band-structure models is mandatory to gain reliable plasmon dispersions as we show for MoS₂ and NbS₂ in Appendix B.

III. RESULTS

In the following we will consider hole and electron doping scenarios with and without spin-orbit coupling. In order to clarify the differences in these situation we provide in Fig. 5 a sketch of all situations. The “hole doping” concentration is chosen in a way that all K and K' (but no Γ) valleys in the conduction band will be populated with holes independently of the in- or exclusion of SOC. In the case of electron doping we will study two different levels: In the “low electron doping” case only the K/K'

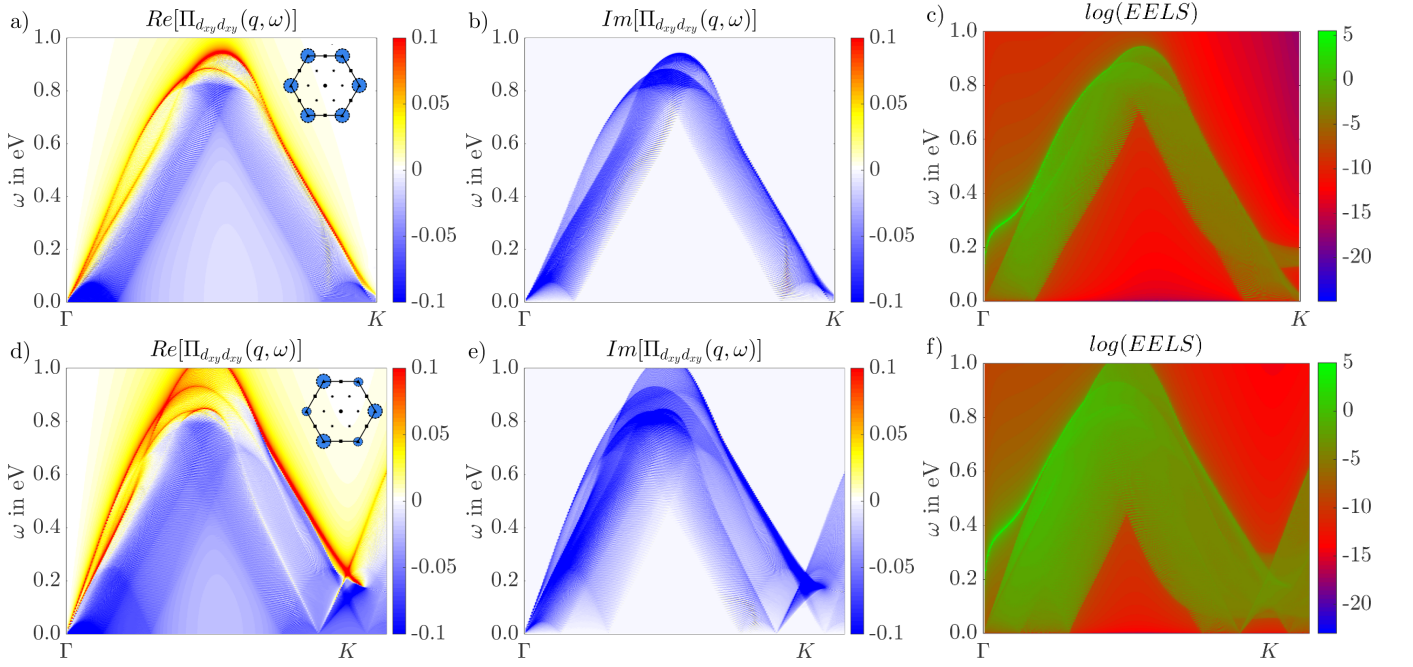


Figure 2: (Color online) Real and imaginary parts of the polarization functions (d_{xy}/d_{xy} channel) and EELS spectra for hole doped MoS₂ without (top row) and with (bottom row) spin orbit coupling. The insets in (a) and (d) illustrate the Fermi surface pockets around K and K' .

valleys of the lowest conduction band are occupied as long as the SOC is excluded while upon inclusion of SOC in addition only one subset of the Σ/Σ' valleys will be occupied. Within the “high electron doping” scenario all K/K' and Σ/Σ' valleys are occupied (with or without SOC).

A. Hole Doping

We fix the chemical potential such that there are holes in the valence band in the K and K' valleys only. The resulting Fermi surfaces consist of circle-like areas around the K points (see Fig. 1), which have mainly $d_{xy}/d_{x^2-y^2}$ character and depend on spin-orbit coupling. Hence, we expect low energy plasmon modes for $\mathbf{q} \approx \Gamma$ (intra-valley) and $\mathbf{q} \approx \mathbf{K}$ (inter-valley), which are possibly influenced by SOC.

In Fig. 2 (a) we show an intensity plot of the real part of the polarization function for scattering within d_{xy} orbitals along the complete path $\Gamma \rightarrow \mathbf{K}$ without SOC⁴⁸. Next to some band-like structures (red) we clearly see the particle-hole continuum [blue, see also Fig. 2 (b)]. In comparison to the corresponding EELS data in Fig. 2 (c), we see that for higher momentum transfers (away from Γ) the EELS maxima closely follow the band-like characteristics of the polarization function. For small momenta around Γ we find a clearly separated band in the EELS spectra, which can not be seen in the real part of the polarization. This separated band arises from the well known \sqrt{q} -dispersive *intra-valley* plasmon mode in 2d²⁹,

while we find a linear-dispersive mode around \mathbf{K} stemming from an *inter-valley* plasmon¹³. These activation laws are consistent with the generalized expression for the plasmon dispersion relation defined by the dielectric function via¹⁵,

$$\omega(q) = \hbar v_F q \sqrt{1 + \frac{[N_0 U(q)]^2}{(1/4) + N_0 U(q)}}, \quad (5)$$

where v_F is the Fermi velocity, N_0 the density of states at the Fermi level and $U(q)$ the macroscopic background screened Coulomb interaction of the undoped system. In the long-wavelength limit ($q \rightarrow 0$), the Coulomb potential remains unscreened, i.e. in leading order $U \propto 1/q$, resulting in a square-root renormalization of the otherwise linear dispersion. However, in the opposite short-range limit, i.e. at the zone boundary, the screened Coulomb potential approaches a constant, and therefore the resulting dispersion of the dielectric function is linear in q , same as the polarization function itself. Thus for momenta away from Γ it is sufficient to study the polarization function to understand how the resulting plasmon dispersion will behave.

Of special interest are damping effects, which are known to attenuate plasmon modes which merge with the particle-hole continuum. Here the square-root mode around Γ behaves in a distinctly different manner compared to the linear modes originating at \mathbf{K} . At sufficiently small momentum transfers $q < q_c$ the square-root modes are more separated from the nearby particle-hole continua [Fig. 2 (c) and (f)], and therefore better pro-

tected from decomposition via hybridization and Landau damping [expressed as non-vanishing imaginary parts of the polarization as shown in Fig. 2 (b) and (e)] compared to the linear modes originating at finite momenta. In contrast, the linear plasmon modes are much closer to their neighboring continua [Fig. 2 (c)], which leads to attenuation effects, reflected in reduced oscillator strength and broadening of the peaks. There is a significant difference in the oscillator strengths of these modes, which can be several orders of magnitude apart as can be seen in Fig. 2 (c) and (f). Hence, in order to clearly detect these linear plasmon modes in experiments, it may prove practical to use a logarithmic scale to shield the dominant square-root mode around $\mathbf{q} = \Gamma$, as shown in Fig. 2 (c) and (f).

When we account for spin-orbit coupling the relative depth of the K and K' pockets shifts. In this case momentum transfer of $\mathbf{q} = \mathbf{K}$ no longer connects points on the Fermi surface belonging to different hole pockets, which results in two clearly visible characteristics in the polarization of Fig. 2 (d): (i) At $\mathbf{q} = \mathbf{K}$ the scattering process is possible only for a finite energy difference, which opens a finite energy gap of ≈ 250 meV. (ii) The Fermi surfaces at K and K' are now of different sizes but can still be connected with slightly smaller and larger \mathbf{q} , resulting in gap-less linear modes originating slightly shifted from K as seen in Fig. 2 (d).

We conclude that the plasmonic features in hole doped MoS_2 are mainly characterized by a square-root mode in the vicinity of the Γ point and additional low contributions at the Brillouin zone edge which disperse linearly when SOC is disregarded. As long as SOC is not taken into account and the K valley is occupied solely this is qualitatively very similar to the plasmonic properties of doped graphene¹³. Upon inclusion of SOC the linear plasmon mode around K is *shifted* leading to a gapped excitation spectra at this point.

B. Electron Doping

The lowest conduction band is characterized by two prominent minima around K and Σ . Without SOC these minima are separated by less than 100 meV which is further reduced by considering SOC. Hence, in contrast to the hole doped case, small variations in the electron doping can change the Fermi-surface topology as shown in the insets of Fig. 3 and Fig. 4. In order to study these changes, we will neglect the SOC for the beginning and choose two doping levels, resulting in Fermi surfaces comparable to the hole doped case (i.e. K valley occupation only) and a surface with additional pockets at Σ , labeled by low- and high-doping respectively (see Appendix A). Since the K valley is mainly described by d_{z^2} orbitals and the Σ valley predominately by d_{xy} and $d_{x^2-y^2}$ states, we focus on corresponding diagonal orbital channels in $\Pi_{\alpha\beta}$ in the following. Off-diagonal elements between d_{z^2} and $d_{xy}/d_{x^2-y^2}$ orbitals are negligible here and off-diagonal

terms between $d_{xy}/d_{x^2-y^2}$ states are very similar to diagonal d_{xy}/d_{xy} and $d_{x^2-y^2}/d_{x^2-y^2}$ combinations. The corresponding polarization functions are shown along the path $\Gamma - \Sigma - K - M - \Gamma$ through the whole Brillouin zone in Fig. 3 and Fig. 4 for d_{z^2} and d_{xy} states, respectively.

Analogous to the hole doped case, we observe in all situations (high and low electron doping) around $\mathbf{q} = \Gamma$ the expected $\omega \propto \sqrt{q}$ plasmonic resonances arising from *intra-valley* scattering (either within the K or the Σ valleys). The structure of the polarization for larger \mathbf{q} can be understood by inspecting the Fermi surface shown in Fig. 1: *Inter-valley* scattering between similar valleys is possible for momentum transfers of $\mathbf{q} = \mathbf{K}$ ($K \leftrightarrow K'$ and $\Sigma \leftrightarrow \Sigma'$ scattering) and $\mathbf{q} = \mathbf{\Sigma}$ and \mathbf{M} ($\Sigma \leftrightarrow \Sigma'$ scattering). Therefore, we expect additional *inter-valley* plasmon branches close to these momenta. In principle $K \leftrightarrow \Sigma$ scattering can be found as well (for instance for $\mathbf{q} = \mathbf{\Sigma}$ or $\mathbf{q} = \mathbf{M}$), but with strongly decreased amplitudes due to vanishing overlap matrix elements $M_{d_{z^2}d_{xy}}$.

Indeed, we find at $\mathbf{q} \approx \mathbf{K}$ in all situations without SOC possible excitations at zero energy. In Fig. 3 (a) and (b) we see the corresponding $K \leftrightarrow K'$ and in Fig. 4 (a) the $\Sigma \leftrightarrow \Sigma'$ modes. As expected, at momentum transfers of $\mathbf{q} = \mathbf{M}$ and $\mathbf{\Sigma}$ we find gap-less linear modes only within the d_{xy} channel for high doping concentrations as shown in Fig. 4 corresponding to $\Sigma \leftrightarrow \Sigma'$ excitations. In contrast, within the low doping case [Fig. 3 (a)] we observe weak and gapped (≈ 0.1 eV) excitations for these momenta originating from $K \leftrightarrow \Sigma$ scattering.

While the SOC has a negligible effect on the d_{z^2} valley at K it splits the $d_{xy}/d_{x^2-y^2}$ valleys at Σ resulting in minima at comparable energies. The corresponding Fermi surface for a single spin component is indicated in the inset of Fig. 4 (b). The six Σ points decompose into two distinct sets, Σ and Σ' . Fermi pockets within each of these subsets are mutually connected by $2\pi/3$ rotations and remain equivalent after inclusion of SOC, while the degeneracy of Σ and Σ' is lifted by SOC. As a consequence, the phase space for $\Sigma \leftrightarrow \Sigma'$ is lost and the gap-less excitations at $\mathbf{q} \approx \mathbf{\Sigma}$ and $\mathbf{q} \approx \mathbf{K}$ must vanish, but $\Sigma \leftrightarrow \Sigma$ scattering processes are still possible. Consequently, we see in the corresponding polarization for the d_{xy} channel with SOC in Fig. 4 (b) gap-less modes only at Γ and \mathbf{M} . Since the Fermi surface around K is not changed drastically upon SOC, the corresponding polarization for the d_{z^2} channel is very similar to the one obtained without SOC [see Fig. 3 (b)].

IV. CONCLUSIONS

We found that the low energy dynamical screening in MoS_2 is controlled by both *inter-* and *intra-valley* scattering processes. These give rise to plasmons with a square-root dispersion at small \mathbf{q} and linear dispersion for higher momentum transfers which connect separate valleys on the Fermi surface. In general, inter-valley plasmon modes are observable, although their oscilla-

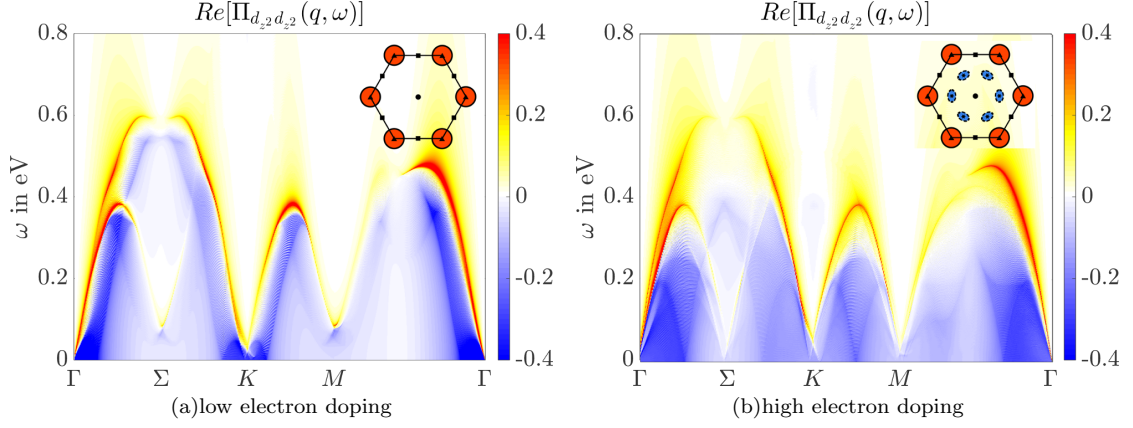


Figure 3: (Color online) Real parts of the polarization functions for d_{z2}/d_{z2} scattering at low and high electron doping concentration without SOC. The insets illustrate the Fermi surfaces.

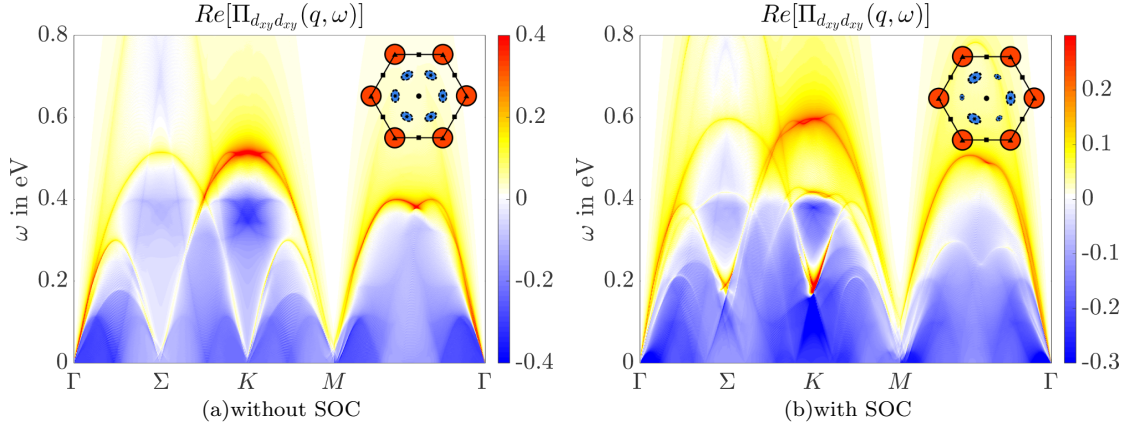


Figure 4: (Color online) Real parts of the polarization functions for d_{xy}/d_{xy} scattering at elevated electron doping concentration (K and Σ valleys are partially occupied) without and with SOC. The insets illustrate the Fermi surfaces.

tor strengths are strongly reduced in comparison to zone center modes. Due to the multi-orbital character of the wave functions and spin-orbit coupling, which leads to spin-valley coupling in monolayer TMDCs, not all *inter-valley* scattering processes are allowed. As a consequence of spin-valley coupling some inter-valley plasmon modes are shifted and gapped out, while the $2\pi/3$ rotation symmetry protects certain low energy modes at \mathbf{M} . We speculate this selective gapping out of collective modes could have consequences for the realization of many-body instabilities towards superconducting or charge density wave phases in monolayer TMDCs.

Acknowledgments: We are grateful for useful discussions with A.V. Balatsky, A. Bill, F. Guinea as well as B. Normand. S.H. would like to thank the Humboldt Foundation for support. This work was supported by the European Graphene Flagship and by the Department of Energy under Grant No. DE-FG02-05ER46240. The numerical computations were carried out on the University of Southern California high performance supercomputer cluster and the Norddeutscher Verbund zur Förderung

des Hoch- und Höchstleistungsrechnens (HLRN) cluster.

Appendix A: Appendix A: Band structure

In Fig. 5 we show the band structure of MoS_2 with spin orbit coupling as resulting from the 3-band tight binding model used in this work. The SOC is included as describe in Ref.²⁶ with $\lambda = 0.1 \text{ eV}$ as the SOC coefficient. All of these three bands are actually of hybrid molybdenum d and sulfur p character with Mo d orbitals being dominant. To get a well defined electronic band structure, we use the Wannier90 package³⁷ in order to properly disentangle these bands. Thereby we use a “frozen” or “inner” energy window, which fixes the highest G_0W_0 valence-band’s energy as well as most parts of the lowest conduction band. The Wannier functions are obtained using projections of atomic Mo $4d$ orbitals onto a limited set of bands in an “outer” energy window including all relevant valence and conduction bands without performing a maximal localization. The limitation of the

Wannierization procedure to these kinds of energy windows ensures that the resulting Wannier functions carry the proper hybrid orbital characters.

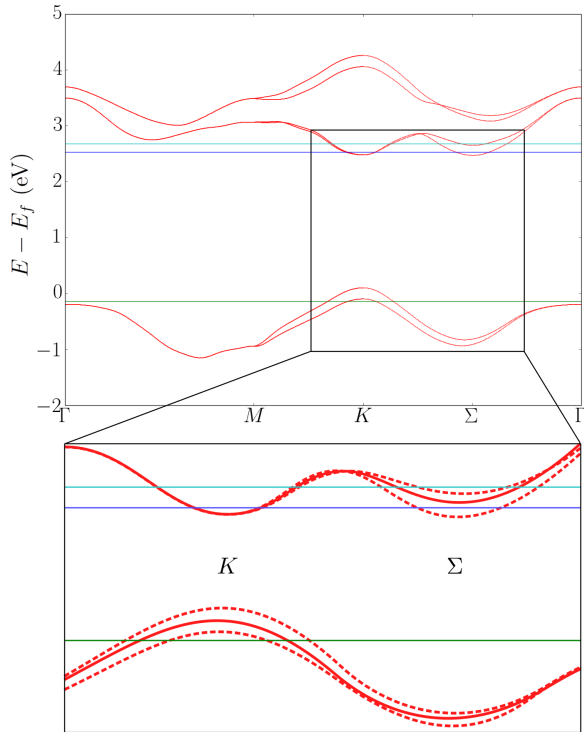


Figure 5: (Color online) Band structure of MoS₂ with spin orbit coupling (top). The two lowest conduction bands and highest valence band are shown. The doping levels discussed in the main text are shown with horizontal lines: green (“hole doping”) $E_f = -0.15$ eV, blue (“low electron doping”) $E_f = 2.52$ eV and cyan (“high electron doping”) $E_f = 2.67$ eV. The lower panel shows a sketch of the splitting due to SOC at K and K' in the valence band and at Σ and Σ' in the lowest conduction band.

Appendix B: Appendix B: Benchmarks

Up to now, there have been basically two theoretical approaches available to study the plasmonic physics in TMDCs. On the one side there are models combining effective $k \cdot p$ descriptions of the quadratic electronic bands around the band gap with an evaluation of the dielectric function within the random phase approximation^{29,30}. On the other side, there are RPA descriptions based on full density functional theory calculations, which include realistic single particle band structures describing the complete Brillouin zone^{32,38–42}.

Here, we add a third approach by utilizing a material-specific low-energy model Hamiltonian derived from ab initio calculations for the undoped material as the basis for the evaluation of dynamical response functions in the electron and hole doped situations. Thereby we gain the possibility to accurately calculate the polarization as well

orbitals	d (Å)	ϵ^∞	γ (Å)
$d_{z^2} d_{z^2}$	9.73	5.41	1.27
$d_{z^2} d_{xy}$	3.91	10.86	1.89
$d_{z^2} d_{x^2-y^2}$	3.96	10.75	1.86
$d_{xy} d_{xy}$	10.25	5.31	1.79
$d_{xy} d_{x^2-y^2}$	6.23	7.58	1.99
$d_{x^2-y^2} d_{x^2-y^2}$	10.22	5.32	1.75

Table I: Parametrization of the orbitally-resolved background screened Coulomb matrix elements for freestanding and unstrained NbS₂ from (constrained) RPA ab initio calculations. In order not to double count the screening effects of the partially occupied highest valence band the corresponding screening effects are neglected here and will be considered by the evaluation of the RPA polarization function as given in Eq. (1).

as the screening functions for the whole Brillouin zone, which enables us to study plasmons at arbitrary momenta as described in the main text.

In Fig. 6 (a) we compare the resulting plasmon dispersions of our ab initio based model (dots) to the models by Scholz et al.²⁹ and Kechedzhi et al.³⁰ (lines) for hole doping with a carrier density of $2 \times 10^{13} \text{ cm}^{-2}$ in the case of MoS₂. In the $k \cdot p$ models a simple *constantly screened* Coulomb interaction of the form $U(q) \propto \frac{1}{\kappa q}$ with $\epsilon_{\alpha\beta}(\mathbf{q}) = \kappa = 5$ is used. As long as we use the same constantly screened Coulomb interaction to evaluate the dielectric function we end up with nearly identical plasmon dispersions compared to those derived from the $k \cdot p$ -models. However, by including the full ab initio derived q dependent dielectric function for the background screening in the undoped case, which arises due to the two dimensional geometry and high energy inter-band polarization processes, we find strongly reduced plasmon energies (green dots). Hence, we conclude that neglecting the material-specific dielectric function $\epsilon_{\alpha\beta}(\mathbf{q})$ within the minimal 3-band model is a severe approximation leading to non-realistic plasmonic properties.

In Fig. 6 (b) we compare our method to full ab initio results for NbS₂⁴¹, which is a metal. Analogous to MoS₂ we use a 3-band tight-binding model which is obtained by projecting ab initio results to Nb d_{z^2} , d_{xy} and $d_{x^2-y^2}$ orbitals. The Coulomb interaction is fitted by the parameters given in Tab. I using the definitions from Ref.³¹. Once again, plasmon dispersions derived from EELS data are shown. Although, the resulting dispersions are on the eV range (for which our model is actually not set-up), we find a remarkable agreement with differences on the order of 100 meV to 200 meV ($\approx 10\%$ to 20%).

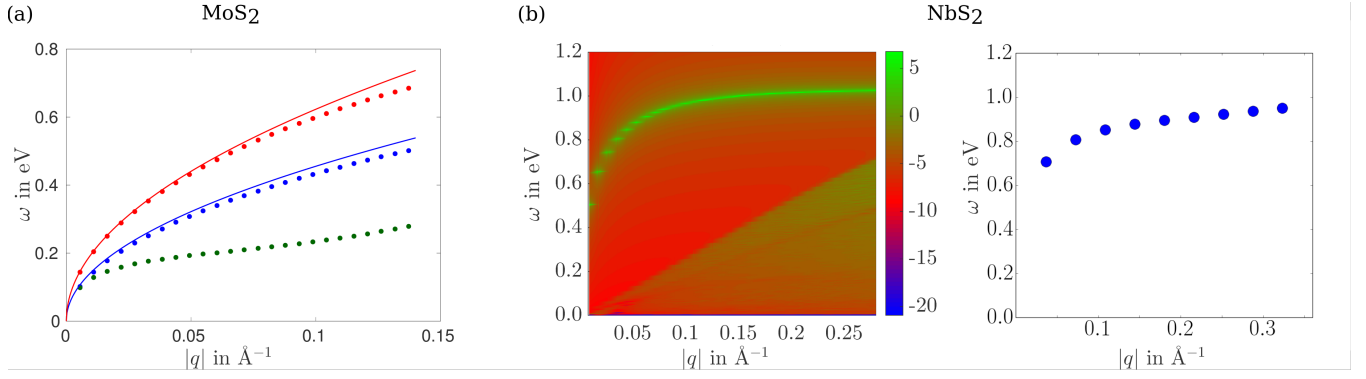


Figure 6: (Color online) **(a)** Plasmon dispersions from our ab initio based model (dots) in comparison with analytic $k \cdot p$ -models by Scholz et al. (blue)²⁹ and Kechedzhi et al. (red)³⁰. In the data by Kechedzhi et al. both spin components and their coupling are included while the data of Scholz et al. includes a single spin component only. Data shown as red (blue) dots results from the ab initio model by using a simple constantly screened Coulomb interaction and the full (spin resolved) polarization function. The data shown as green dots arise from the complete ab initio model. **(b)** Plasmon dispersions for undoped NbS₂ from (right) full ab initio calculations from Ref.⁴¹ and (left) EELS data obtained from our ab initio based model.

-
- * R. E. Groenewald and M. Rösner contributed equally to this work.
- ¹ F. H. L. Koppens, D. E. Chang, and F. J. García de Abajo, *Nano Letters* **11**, 3370 (2011).
 - ² Q. Bao and K. P. Loh, *ACS Nano* **6**, 3677 (2012).
 - ³ A. N. Grigorenko, M. Polini, and K. S. Novoselov, *Nature Photonics* **6**, 749 (2012).
 - ⁴ F. J. García de Abajo, *ACS Photonics* **1**, 135 (2014).
 - ⁵ R. H. Ritchie, *Physical Review* **106**, 874 (1957).
 - ⁶ N. Bhukal, Priya, and R. K. Moudgil, *Physica E: Low-dimensional Systems and Nanostructures* **69**, 13 (2015).
 - ⁷ Y. Liu, R. F. Willis, K. V. Emtsev, and T. Seyller, *Physical Review B* **78**, 201403 (2008).
 - ⁸ L. Ju, B. Geng, J. Horng, C. Girit, M. Martin, Z. Hao, H. A. Bechtel, X. Liang, A. Zettl, Y. R. Shen, and F. Wang, *Nature Nanotechnology* **6**, 630 (2011).
 - ⁹ B. Wunsch, T. Stauber, F. Sols, and F. Guinea, *New Journal of Physics* **8**, 318 (2006).
 - ¹⁰ E. H. Hwang and S. Das Sarma, *Physical Review B* **75**, 205418 (2007).
 - ¹¹ S. Gangadharaiyah, A. M. Farid, and E. G. Mishchenko, *Physical Review Letters* **100**, 166802 (2008).
 - ¹² T. Stauber, *Journal of Physics: Condensed Matter* **26**, 123201 (2014).
 - ¹³ T. Tudorovskiy and S. A. Mikhailov, *Physical Review B* **82**, 073411 (2010).
 - ¹⁴ H. Rietschel and L. J. Sham, *Physical Review B* **28**, 5100 (1983).
 - ¹⁵ A. Bill, H. Morawitz, and V. Z. Kresin, *Physical Review B* **68**, 144519 (2003).
 - ¹⁶ R. Akashi and R. Arita, *Physical Review Letters* **111**, 057006 (2013).
 - ¹⁷ A. Linscheid, A. Sanna, and E. K. U. Gross, *arXiv:1503.00977 [cond-mat]* (2015), *arXiv: 1503.00977*.
 - ¹⁸ J. van Wezel, R. Schuster, A. König, M. Knupfer, J. van den Brink, H. Berger, and B. Büchner, *Physical Review Letters* **107**, 176404 (2011).
 - ¹⁹ A. König, K. Koepf, R. Schuster, R. Kraus, M. Knupfer, B. Büchner, and H. Berger, *EPL (Europhysics Letters)* **100**, 27002 (2012).
 - ²⁰ A. König, R. Schuster, M. Knupfer, B. Büchner, and H. Berger, *Physical Review B* **87**, 195119 (2013).
 - ²¹ K. Kalantar-zadeh, J. Z. Ou, T. Daeneke, M. S. Strano, M. Pumera, and S. L. Gras, *Advanced Functional Materials* **25**, 5086 (2015).
 - ²² K. Kalantar-zadeh and J. Z. Ou, *ACS Sensors* (2015), 10.1021/acssensors.5b00142.
 - ²³ J. B. Maurya, Y. K. Prajapati, V. Singh, J. P. Saini, and R. Tripathi, *Optical and Quantum Electronics* **47**, 3599 (2015).
 - ²⁴ E. Cappelluti, R. Roldán, J. A. Silva-Guillén, P. Ordejón, and F. Guinea, *Physical Review B* **88**, 075409 (2013).
 - ²⁵ C.-H. Chang, X. Fan, S.-H. Lin, and J.-L. Kuo, *Physical Review B* **88**, 195420 (2013).
 - ²⁶ G.-B. Liu, W.-Y. Shan, Y. Yao, W. Yao, and D. Xiao, *Physical Review B* **88**, 085433 (2013).
 - ²⁷ Z. Y. Zhu, Y. C. Cheng, and U. Schwingenschlögl, *Physical Review B* **84**, 153402 (2011).
 - ²⁸ L. Chu, H. Schmidt, J. Pu, S. Wang, B. Özyilmaz, T. Takenobu, and G. Eda, *Scientific Reports* **4**, 7293 (2014).
 - ²⁹ A. Scholz, T. Stauber, and J. Schliemann, *Physical Review B* **88**, 035135 (2013).
 - ³⁰ K. Kechedzhi and D. S. L. Abergel, *Physical Review B* **89**, 235420 (2014).
 - ³¹ A. Steinhoff, M. Rösner, F. Jahnke, T. O. Wehling, and C. Gies, *Nano Letters* **14**, 3743 (2014).
 - ³² Y. Liang and L. Yang, *Physical Review Letters* **114**, 063001 (2015).
 - ³³ M. Rösner, E. Şaşıoğlu, C. Friedrich, S. Blügel, and T. O. Wehling, *Physical Review B* **92**, 085102 (2015).
 - ³⁴ F. Roth, A. König, J. Fink, B. Büchner, and M. Knupfer, *Journal of Electron Spectroscopy and Related Phenomena* **195**, 85 (2014).
 - ³⁵ H. Yan, T. Low, W. Zhu, Y. Wu, M. Freitag, X. Li, F. Guinea, P. Avouris, and F. Xia, *Nature Photonics* **7**, 394 (2013).
 - ³⁶ A. Principi, G. Vignale, M. Carrega, and M. Polini, *Physical Review B* **88**, 195405 (2013).
 - ³⁷ A. A. Mostofi, J. R. Yates, Y.-S. Lee, I. Souza, D. Vanderbilt, and N. Marzari, *Computer Physics Communications* **178**, 685 (2008).
 - ³⁸ P. Johari and V. B. Shenoy, *ACS Nano* **5**, 5903 (2011).
 - ³⁹ M. N. Faraggi, A. Arnau, and V. M. Silkin, *Physical Review B* **86**, 035115 (2012).
 - ⁴⁰ P. Cudazzo, M. Gatti, and A. Rubio, *Physical Review B* **86**, 075121 (2012).
 - ⁴¹ K. Andersen and K. S. Thygesen, *Physical Review B* **88**, 155128 (2013).
 - ⁴² P. Cudazzo, M. Gatti, and A. Rubio, *Physical Review B* **90**, 205128 (2014).
 - ⁴³ G. Kresse and J. Hafner, *Physical Review B* **47**, 558 (1993).
 - ⁴⁴ G. Kresse and J. Furthmüller, *Computational Materials Science* **6**, 15 (1996).
 - ⁴⁵ C. Friedrich, S. Blügel, and A. Schindlmayr, *Physical Review B* **81**, 125102 (2010).
 - ⁴⁶ “The Juelich FLEUR project,” (2014).
 - ⁴⁷ In all ab initio calculations we used an interlayer separation of 35 Å. The G_0W_0 calculations are performed with the Vienna ab initio simulation package (VASP)^{43,44}, while the Coulomb matrix elements are obtained from the SPEX code⁴⁵ with FLAPW input from the FLEUR code⁴⁶ as described in³¹. For the involved Wannier projections we use the Wannier90 package³⁷. See supplemental material for further details.
 - ⁴⁸ Here we apply Γ centered Monkhorst-Pack 720×720 k -grids and use a broadening of $i\delta = 0.0005i$. The doping concentration is adjusted by rigid shifts of the Fermi energy, which change the Fermi functions accordingly. All calculations are carried out for $T = 0$ K. Furthermore, we restricted the λ_1 and λ_2 summations to the partially occupied band only in order to avoid double counting problems within the definition of the total polarization function and not to overload the resulting plots.